Electronic Supporting Information

Ni2P Active Site Ensembles Tune Electrocatalytic Nitrate Reduction Selectivity

Emily Nishiwaki[1], Peter S. Rice[2], Ding-Yuan Kuo[1], Florence Y. Dou[1], Anthony Pyka[3], Bryce Reis[3], Hao A. Nguyen[1], Eric M. Stuve[3], Simone Raugei[2], Brandi M. Cossairt[1]*

[1] *Department of Chemistry, University of Washington, Seattle, WA 98195, United States*

[2] *Pacific Northwest National Laboratory, Richland, Washington, WA 99352, United States*

[3] *Department of Chemical Engineering, University of Washington, Seattle, WA 98195, United States*

*Corresponding author: Brandi M. Cossairt (cossairt@uw.edu)

I.   Synthetic, Electrochemical, and Product Quantification Methods

Chemicals. $NiCl_2$ and tris(diethylamino)phosphine were used as received. Oleylamine (90%) was purified via distillation. All reagents were dried and kept under inert conditions.

Synthesis of Ni₂P nanocrystals. Ni_2P nanocrystals were synthesized with a Schlenk line under inert conditions according to previous methods found in our lab.[1] 5.46 mmol of $NiCl_2$ (1 eq) and 109.5 mmol of oleylamine (21 eq) were degassed at 120 °C for 60 minutes. The temperature was lowered to 50 °C and 21.6 mmol of tris-diethyl amino phosphine (4 eq) was injected. The temperature was ramped to 250 °C and was held for 60 minutes. The nanoparticles were purified via centrifugation in the glove box with a pentane/IPA mixture (4x) at 7800rpm and toluene/acetonitrile mixture (1x).

Deposition of Ni₂P on Carbon Black Vulcan XC-72. Previously reported methods were used with modifications.[2] 30 wt% of Ni_2P (excluding ligand mass) was deposited onto Vulcan carbon. For the deposition, 100 mg of Vulcan carbon was dried in a 100 mL Schlenk flask at 100 °C overnight. Vulcan carbon was transferred into a glovebox and dispersed in 20 mL pentane then sonicated for 5 min. The carbon dispersion was stirred at 1500 rpm and 7.3 mL of a 5 mg/mL Ni_2P stock solution in chloroform was added dropwise. The mixture was then sonicated for 5 min and transferred back to a glovebox stirring at 1500 rpm overnight. The next day, 15 mL of acetonitrile was added slowly while the suspension was stirred at 800 rpm. The mixture was centrifuged at 7830 rpm for 10 min and the clear supernatant was decanted. The precipitate (Ni_2P/C) was re-dispersed in 10 mL isopropanol.

The Ni_2P/C was annealed at 450 °C for 2 hours under 95:5 N_2:H_2 gas. All sample handling was done under inert conditions to preserve the Ni_2P nanocrystals.

Electrochemical Methods. 0.1 M phosphate buffer (pH 6.9) was prepared with a 1:1 ratio of KH_2PO_4: K_2HPO_4. All measurements were conducted with an A Ag/AgCl reference electrode and Pt counter electrode and a Nafion membrane separating the cathodic and anodic compartments. Carbon paper working electrodes (FuelCell Store, AvCarb MGL190) with Ni_2P nanocrystals were prepared by sonicating and then immediately drop-casting 30 μL of a 10mg/mL solution of Ni_2P/C onto a 1x1cm carbon paper electrode (90 μg of Ni_2P on each electrode). Carbon paper electrodes were 0.88 cm^2 ± 0.1 cm^2.

Calibration curve and quantification of NH₃. NH_3 was quantified via the indophenol blue method using salicylic acid instead of phenol.[3] 100 mM $(NH_4)_2SO_4$ solution was prepared with 0.1 M phosphate buffer

solution and $(NH_4)_2SO_4$. 5 mM $(NH_4)_2SO_4$ solution was prepared by mixing 0.5 mL of 100 mM $(NH_4)_2SO_4$ solution with 9.5 mL of 0.1 M phosphate buffer. 2500, 1250, 625, 312.5, 156.25 μM of $(NH_4)_2SO_4$ solutions were prepared by sequential dilution with 0.1 M phosphate buffer. A 0 μM of $(NH_4)_2SO_4$ solution was also prepared (100 μL). The reference solutions were diluted 10 times with Millipore water by taking 100uL of original solution and adding 900uL of Millipore water. After dilution, the concentration of reference solutions were as followed: 250, 125, 62.5, 31.25, 15.625 μM of $(NH_4)_2SO_4$ with 20 μM of potassium phosphate. The actual concentration of NH_3 should be doubled: 500, 250, 125, 62.5, 31.25, 0 μM.

To each tube, 1000 μL 1 M NaOH solution was added (1000 μL reference solution: 1000 μL 1 M NaOH. The tubes were shaken vigorously. 500 μL of coloring agent, 50 μL of 0.034 M sodium nitroprusside dihydrate (Sigma-Aldrich, ≥99%), and 50 μL of NaClO solution (4.00-4.99 % chlorine, Sigma-Aldrich, reagent grade) were swirled to ensure a homogeneous mixture, and then added to the 15 mL centrifugation tube sequentially. The coloring agent was prepared by dissolving 3.6 mmol of salicylic acid (Sigma-Aldrich, ≥99.0%) and 1.8 mmol of potassium sodium tartrate tetrahydrate (Sigma Aldrich, 99%) in 3.6 mL of 1 M NaOH solution and diluted it to 10 mL with Millipore water.

For product quantification, the electrolyte was diluted to an appropriate concentration within the calibration curve range with 0.1 M phosphate buffer. To that, the same amounts of NaOH, coloring agent, sodium nitroprusside, and NaClO were added. UV-vis spectrometry was used to measure the absorption of the colored complex at 660 nm to construct the calibration curve and calculate the concentration of NH_3 in an electrolyte.

Calibration curve and quantification of NO_2^-. NO_2^- was quantified via the Griess method, as reported by previous studies.[4] 0.2 % N-(1-naphthyl)ethylenediamine dihydrochloride solution was prepared by dissolving 0.1 g of N-(1-naphthyl)ethylenediamine dihydrochloride (Merck, ACS grade) in 50 mL of Millipore water. The 2 % sulfanilamide solution was prepared by dissolving 1 g of sulfonamide (Sigma-Aldrich, 98%) and 2.94 g of H_3PO_4 in 50 mL of Millipore water.

1 mmol of KNO_2 (85.1 mg) was dissolved in 10 mL of 100 mM phosphate buffer solution. 1 mM KNO_2 solution was prepared by mixing 0.1 mL of 100 mM KNO_2 solution with 9.9 mL of 0.1 M phosphate buffer. 500, 250, 125, 62.5, 31.25, 0 μM of KNO_2 solutions were prepared by sequential dilution with 0.1 M phosphate buffer. 500 μL reference solution and 500 μL Millipore water were added to a 15 mL centrifugation tube. The tube was shaken vigorously. 1 mL of 2 % sulfanilamide solution was added, and the tube was incubated for 5 min at RT, protected from light. Then 1 mL of 0.2 % N-(1-naphthyl)ethylenediamine dihydrochloride solution was added, and the tube was further incubated for 10 min at RT, protected from light. The final concentrations are 500, 250, 125, 62.5, 31.25, 0 μM before any dilution by water.

For product quantification, the electrolyte was diluted to an appropriate concentration within the calibration curve range with 0.1 M phosphate buffer. To that, the same amounts of sulfanilamide solution and N-(1-naphthyl)ethylenediamine dihydrochloride solution were added. UV-vis spectrometry was used to measure the absorption of the colored complex at 540 nm to construct the calibration curve and calculate the concentration of NO_2^- in an electrolyte.
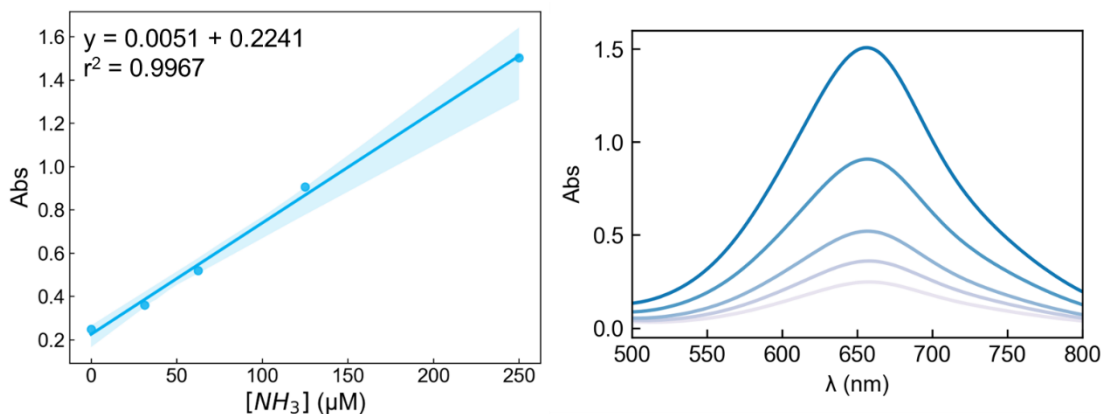
Figure S1. NH$_3$ calibration curve and corresponding UV-visible absorption spectra.
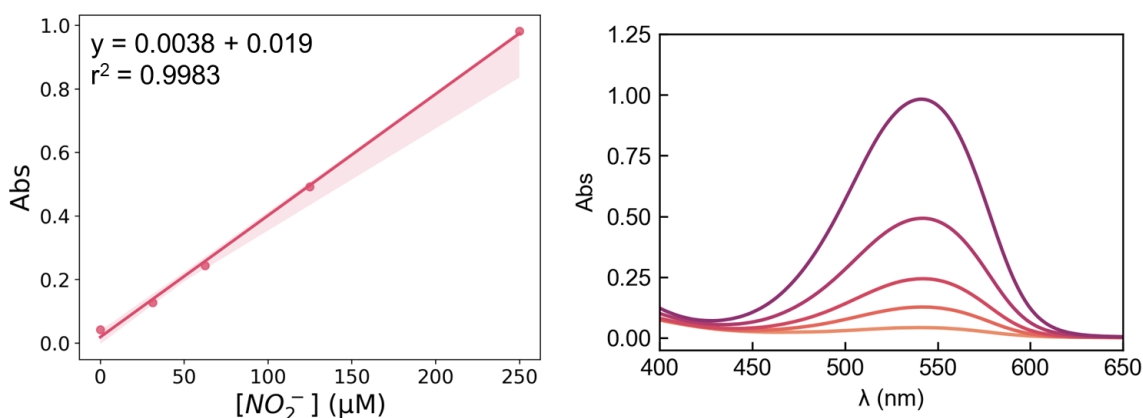

Figure S2. NO$_2^-$ calibration curve and corresponding UV-visible absorption spectra.

Calculation of product faradaic efficiency. Faradaic efficiency is calculated by:

$$FE_{product} = \frac{c_{product}}{c_{total}} = \frac{c_{product}}{i * t}$$

where c is charge, *i* is current, and t is the time. The total charge is the integration of the chronoamperometry trace.

The charge associated with a certain product is calculated by:

$$c_{product} = [product] * V_{electrolyte} * n * DF$$

where V is the volume, n is the number of electrons required for the reaction (n=2 for NO$_2^-$, n=8 for NH$_3$), and DF is the dilution factor of the electrolyte for quantification.

II. Ni₂P/C Catalyst characterization
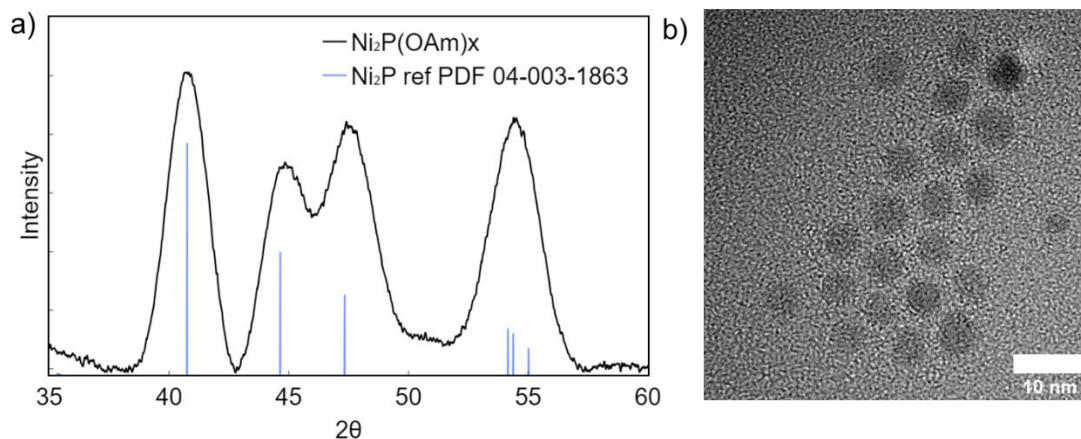
Figure S3. a**)** XRD and b**)** TEM images of Ni₂P nanocrystals (5.4 ± 0.8 nm) capped by oleylamine ligands. The reported size is the diameter of the particles. The diameter of 200+ particles were measured in two orthogonal directions for each particle (400+ total measurements). The measurements were averaged and the "±" indicates the standard deviation.
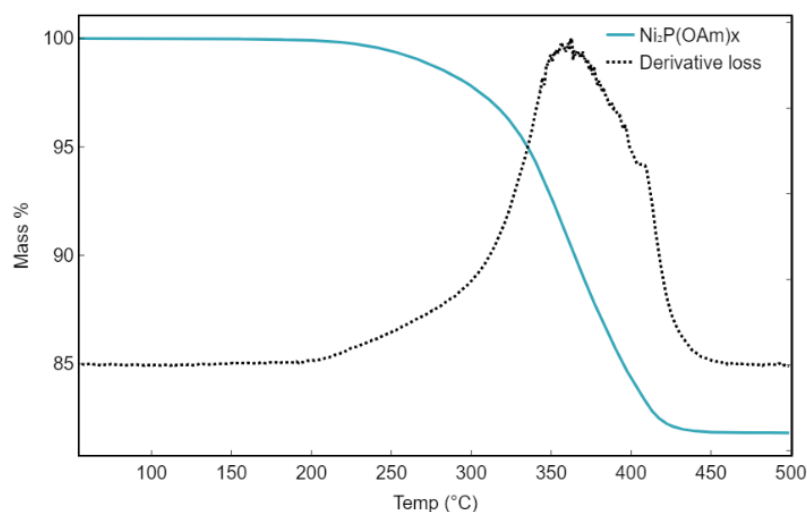

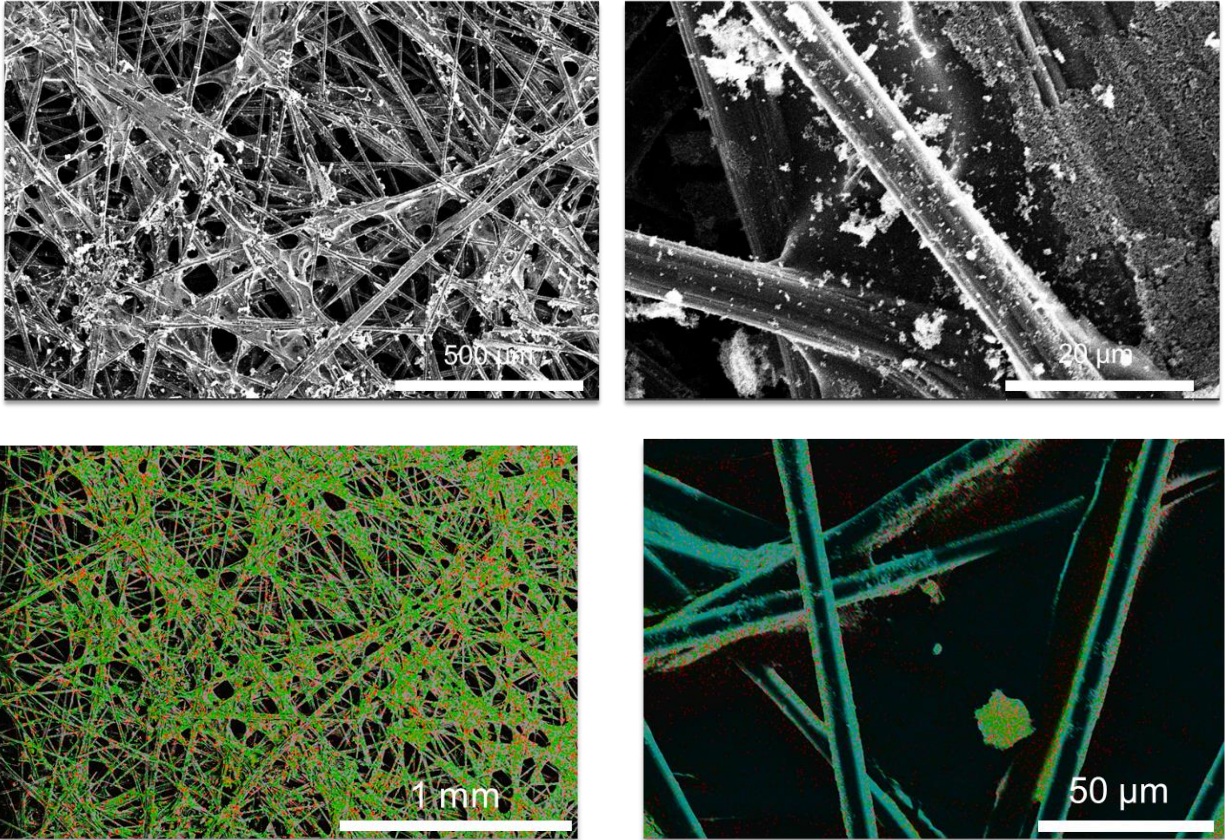**Figure S4.** TGA of Ni₂P nanocrystals. The mass % of the nanocrystals is 81.8%.

Figure S5. SEM of Ni$_2$P electrode. Green indicates phosphorus, red indicates Ni. The long, web-like structure is the carbon paper electrode and the dispersed white powder-like features is Vulcan carbon with deposited Ni$_2$P nanocrystals.
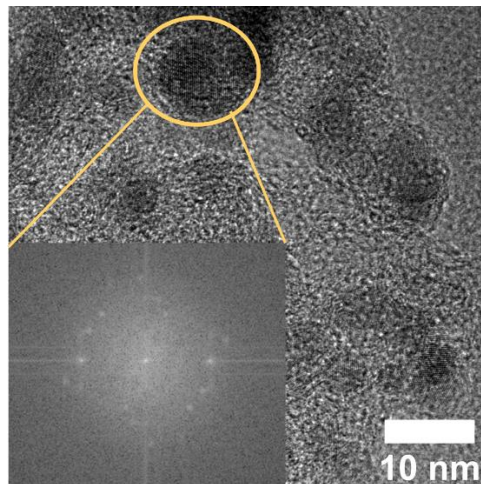

Figure S6. A sample FFT image of a Ni$_2$P nanocrystal. Measurements of a sample of nanocrystals showed a predominant lattice spacing of 0.22 nm, indicating the majority of particles are (111)-faceted.
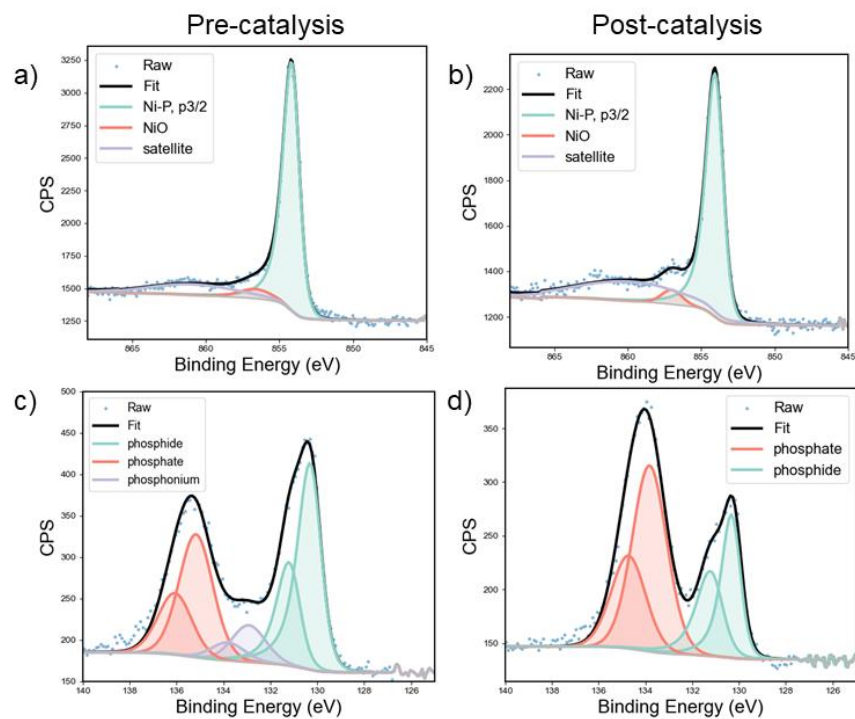
Figure S7. Ni 2p$_{3/2}$ **(a, b)** and P 2p **(c, d)** XPS spectra of Ni$_2$P/C on carbon fiber, pre and post catalysis. Phosphonium signal is present from the original synthesis, which is a known by-product in the procedure.[1] The change in the ratio to of the phosphate and phosphide peaks is attributed mainly to leftover electrolyte (KH$_2$PO$_4$/K$_2$HPO$_4$) on the electrode that could not be washed off easily.

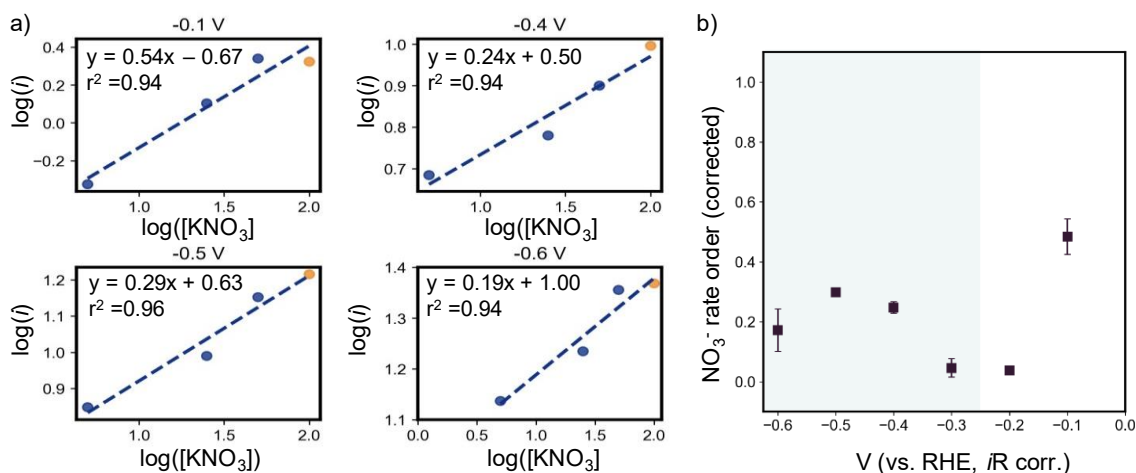## III.   Ni$_2$P/C Electrocatalytic measurements

Figure S8. H-cell set up.

Figure S9. a) Sample log(*i*) vs. log([KNO₃] plots at a range of potentials. The 100 mM datapoint is corrected to only account for i_{NO3RR} (orange), which was identified by product quantification from bulk electrolysis experiments **b)** Corresponding rate order plot only with voltages where i_{NO3RR} is corrected.

Figure 2b is a plot of the rate order vs potential (i.e., the slopes of the log(*i*) vs log([KNO₃] plots at a range of potentials) under the assumption that 100% of the current is toward the NO₃RR. We acknowledge that is not the case and that HER is a competing side reaction. Therefore, we correct for this to the best of our ability and demonstrate a similar quantitative trend in Figure S9b to the one observed in Figure 2b.

The datapoints in S9b are the slopes of log(*i*) vs log([KNO₃] plots (such as the ones in Figure S9a), where the current at 100 mM KNO₃ (labeled in orange) is multiplied by the total faradaic efficiency of the NO₃RR products measured at that potential (Figure 2c). For example, at -0.1 V vs RHE, the total FE toward NH₃ and NO₂ is 83.6%. The *i* measured at this potential is multiplied by a factor of 0.836 to isolate i_{NO3} and the NO₃ rate order. This analysis was propagated at all the potentials where products were quantified (-0.1 to -0.6 V vs RHE).
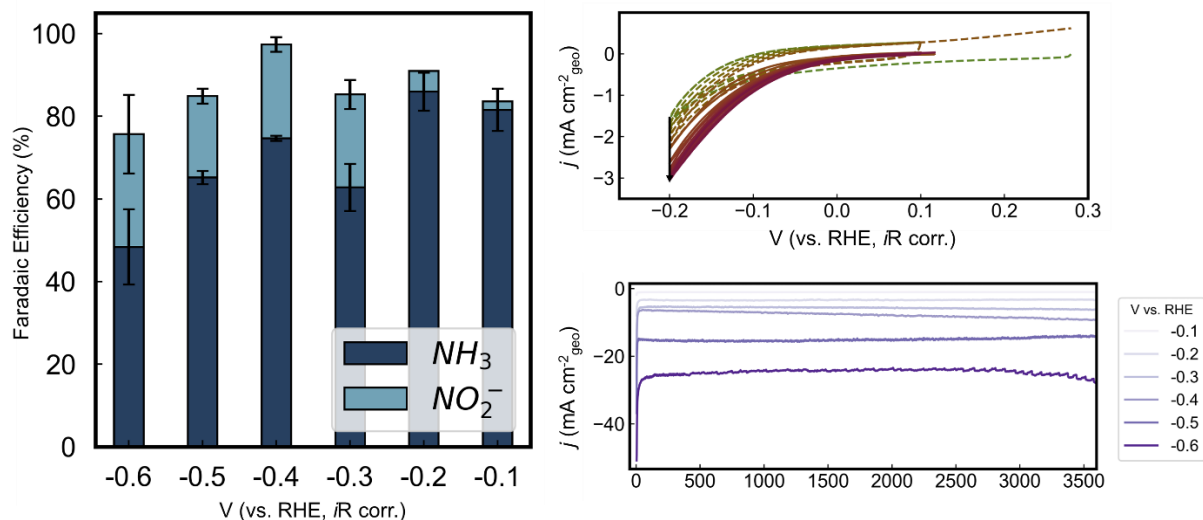
Figure S10. **a)** Ni$_2$P/C selectivity for NO$_3$RR from -0.1 – -0.6 V vs. RHE. **b)** Activation of Ni$_2$P/C prior to chronoamperometry by taking CV from 0.1 V to -0.2 V vs. RHE at 50 mV/s (6x) and 5 mV/s (6x). Dashed lines indicate scans at 50 mV/s, solid lines indicate scans at 5 mV/s. Activation was performed for every electrode until the CV stabilized. **c)** Chronoamperometry of Ni$_2$P/C from -0.1–-0.6 V vs RHE.
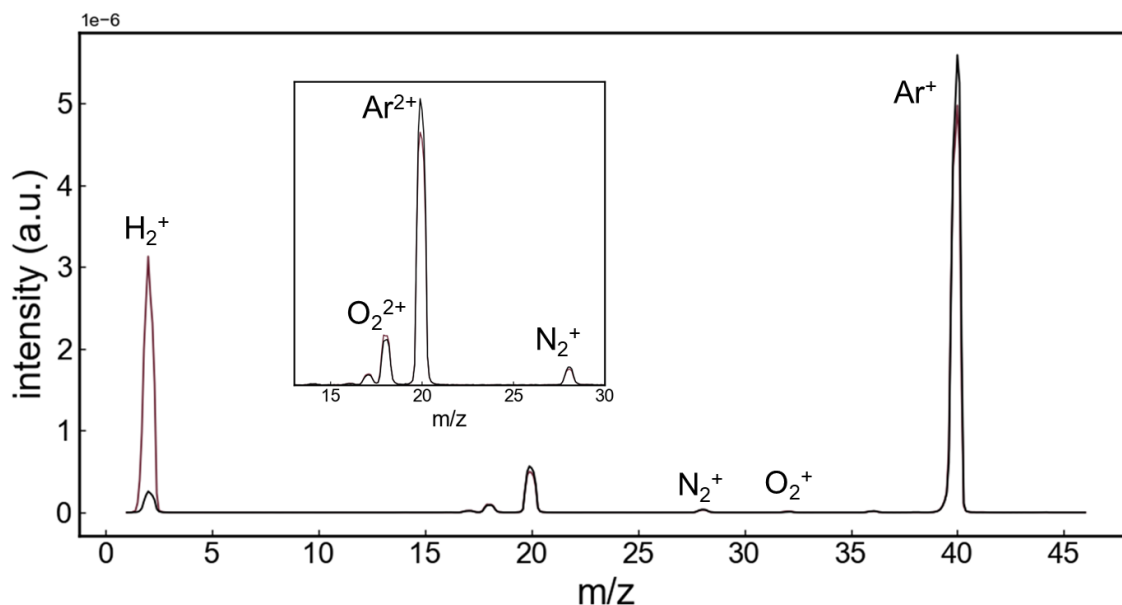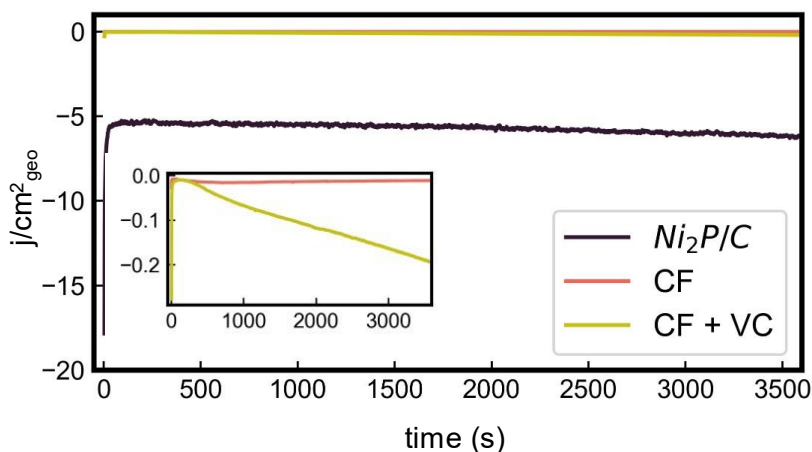

Figure S11. Mass spectrometry measurements taken after 1 hour of bulk electrolysis at -0.6V vs RHE. Significant increase in the H$_2$ signal while no change in the N$_2$ signal from the background indicates H$_2$ production and negligible N$_2$ production. The increase in O$_2$ signal is due to OER occurring at the counter electrode.

Material	Total charge passed (c)
Carbon Fiber (CF)	-0.05
Carbon Fiber (CF) + Vulcan carbon (VC)	-0.38
Ni_2P/C	-21.1

Figure S12. Chronoamperometry and charge passed at -0.3V vs RHE. Negligible product formation without catalyst observed at this potential.

V	-0.6	-0.5	-0.4	-0.3	-0.2	-0.1
-0.6		Y	Y	Y	Y	N
-0.5			Y	N	N	N
-0.4				Y	N	Y
-0.3					N	N
-0.2						N
-0.1						

Table S1. T-test results of total NO_3RR Faradaic efficiencies at different potentials.

V	-0.6	-0.5	-0.4	-0.3	-0.2	-0.1
-0.6		Y	Y	Y	Y	Y
-0.5			Y	N	Y	Y
-0.4				Y	Y	Y
-0.3					Y	Y
-0.2						N
-0.1						

Table S2. T-test results of NH_3 Faradaic efficiencies at different potentials.

V	-0.6	-0.5	-0.4	-0.3	-0.2	-0.1
-0.6		N	N	N	Y	Y
-0.5			N	N	Y	Y
-0.4				N	Y	Y
-0.3					Y	Y
-0.2						Y
-0.1						

Table S3. T-test results of NO_2^- Faradaic efficiencies at different potentials. The bolded line demarcates the H_2O versus $H_2PO_4^-$ mediated regions.
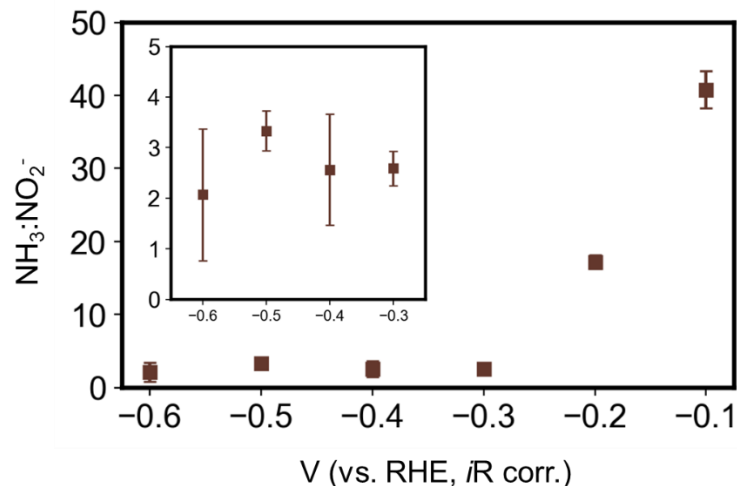
Figure S13. Ratio of $NH_3:NO_2^-$ Faradaic efficiency across all measured potentials.

IV.   Computation

Computational Methods.

All spin-polarized DFT calculations were done using the Quantum ESPRESSO[5] package (v7.1). Exchange-correlation effects are described using the Perdew−Burke−Ernzerhof (PBE) functional.[6] We used the semi-empirical Grimme's D2 method[7] to treat van der Waals (vdW) interactions. The bonding environment of each system is described under the projector augmented wave method (PAW)[8]. The expansion of valence wave functions has been accounted for with a plane wave cut-off energy of 680 eV. All simulations used a 3x3x1 Γ-centered Monkhorst-Pack[9] k-point integration of the Brillouin zone. Surface reactions are modeled using an 8-layer periodically repeated hexagonal supercell (11.8 Å x 11.8 Å x 41.6 Å) belonging to the P$\bar{6}$2m space group to model the coverage effect of surface adsorbates. A 25 Å vacuum space was employed to prevent spurious interactions between the periodically repeated images. Atomic coordinates were relaxed using the Broyden–Fletcher–Goldfarb–Shanno[10] (BFGS) algorithm until the Hellmann-Feynman forces on all relaxed atoms fell below 0.03 eV/Å. The electron occupancies were determined for geometry optimization using the Gaussian smearing method with a smearing value of 0.1 eV. The aqueous reaction medium was described with a dielectric constant of $\varepsilon_0 = 80.0$ using the self-consistent continuum solvation method implemented in the Quantum ESPRESSO ENVIRON.[11,12] The Ni$_2$P(0001) slab with the Ni$_3$P$_2$ surface termination was used to provide a point of reference with our previous work,[13] which explored the influence of co-adsorbed diazonium salts on hydrogen adsorption free energy.

The free energies under an applied potential are calculated using the computational hydrogen electrode (CHE) method developed by Norskøv and co-workers.[14] Within the CHE framework, we assume that protons (H⁺) and electrons (e⁻) are at equilibrium with hydrogen gas (H₂(g)) at 1 atm, 298 K:

$$\mu_{H^+} + \mu_{e^-} = \frac{1}{2}\mu_{H_2}$$

where μ_{H^+}, μ_{e^-}, and μ_{H_2} are the chemical potentials of a proton, electron, and hydrogen, respectively.

The reaction free energy is then calculated as:

$$\Delta G = \Delta E^{DFT} + \Delta ZPVE - T\Delta S + |ne^-|U_{RHE}$$

Where, ΔE^{DFT}, $\Delta ZPVE$ and ΔS are the changes of the DFT reaction energy, zero-point vibrational energy, and entropy, respectively. U_{RHE} is the free energy contribution related to the applied electrode potential U vs the reversible hydrogen electrode (RHE). At pH = 6.9 the relation to the standard hydrogen electrode (SHE) becomes:

$$U_{RHE} = U_{SHE} + k_B T ln(10)pH = U_{SHE} + 0.059pH$$

Here, the applied potential and the concertation correction only influence the chemical potential of steps involving H⁺/e⁻ transfer, where T = 300 K and k_B is the Boltzmann constant.

In this work, we consider the following intermediates adsorbed onto the Ni₂P surface: NO₃*, NO₂*, NO*, NOH*, NH₂O*, NHOH*, NH*, NH₂*, NH₃*, N*, NHO* and NH₂OH*. These species are present along the N*, NHOH* and NH₂OH* pathways for the nitrate reduction reaction (NO₃RR) to ammonia outlined by Guo and co-workers[15] on copper surfaces:

N* pathway

$$G_1 = (G_{NO_3*} + +G_H) - (G_{HNO_3(aq)} + G_*)$$

$$G_2 = (G_{NO_2*} + G_{H_2O}) - (G_{NO_3(aq)} + 2G_H)$$

$$G_3 = (G_{NO*} + G_{H_2O}) - (G_{NO_2*} + 2G_H)$$

$$G_4 = (G_{N*} + G_{H_2O}) - (G_{NO*} + 2G_H)$$

$$G_5 = (G_{NH*}) - (G_{N*} + G_H)$$

$$G_6 = (G_{NH_2*}) - (G_{NH*} + G_H)$$

$$G_7 = (G_{NH_3*}) - (G_{NH_2*} + G_H)$$

$$G_8 = (G_{NH_3} + G_*) - G_{NH_3*}$$

NH₂OH* pathway

$$G_1 = (G_{NO_3*} + +G_H) - (G_{HNO_3(aq)} + G_*)$$

$$G_2 = (G_{NO_2*} + G_{H_2O}) - (G_{NO_3(aq)} + 2G_H)$$

$$G_3 = (G_{NO*} + G_{H_2O}) - (G_{NO_2*} + 2G_H)$$

$$G_{4'} = (G_{NOH*}) - (G_{NO*} + G_H)$$

$$G_{5'} = (G_{NHOH*}) - (G_{NOH*} + G_H)$$

$$G_{6'} = (G_{NH_2OH*}) - (G_{NHOH*} + G_H)$$

$$G_{7'} = (G_{NH_2*} + G_{H_2O}) - (G_{NH_2OH*} + G_H)$$

$$G_7 = (G_{NH_3*}) - (G_{NH_2*} + G_H)$$

$$G_8 = (G_{NH_3} + G_*) - G_{NH_3*}$$

NHOH* pathway

$$G_1 = (G_{NO_3*} + +G_H) - (G_{HNO_3(aq)} + G_*)$$

$$G_2 = (G_{NO_2*} + G_{H_2O}) - (G_{NO_3(aq)} + 2G_H)$$

$$G_3 = (G_{NO*} + G_{H_2O}) - (G_{NO_2*} + 2G_H)$$

$$G_{4'} = (G_{NOH*}) - (G_{NO*} + G_H)$$

$$G_{5'} = (G_{NHOH*}) - (G_{NOH*} + G_H)$$

$$G_{6'} = (G_{NH*} + G_{H_2O}) - (G_{NOH*} + 2G_H)$$

$$G_7 = (G_{NH_2*}) - (G_{NH*} + G_H)$$

$$G_8 = (G_{NH_3*}) - (G_{NH_2*} + G_H)$$
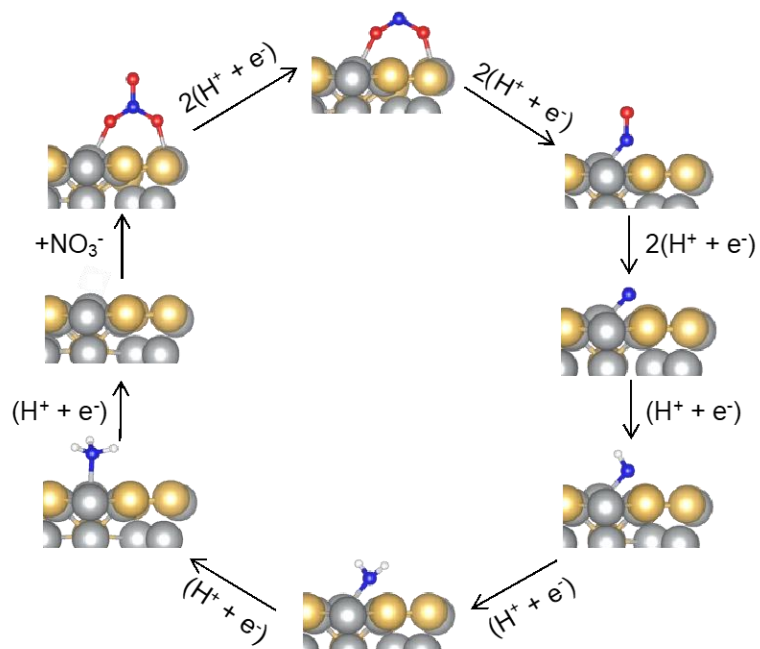
$$G_9 = (G_{NH_3} + G_*) - G_{NH_3*}$$

Figure S13. Proposed mechanism for the electrochemical nitrate reduction reaction (NO₃RR) on Ni₂P nanocrystals going from nitrate (NO₃⁻) to ammonium (NH₄⁺) at pH = 6.9.
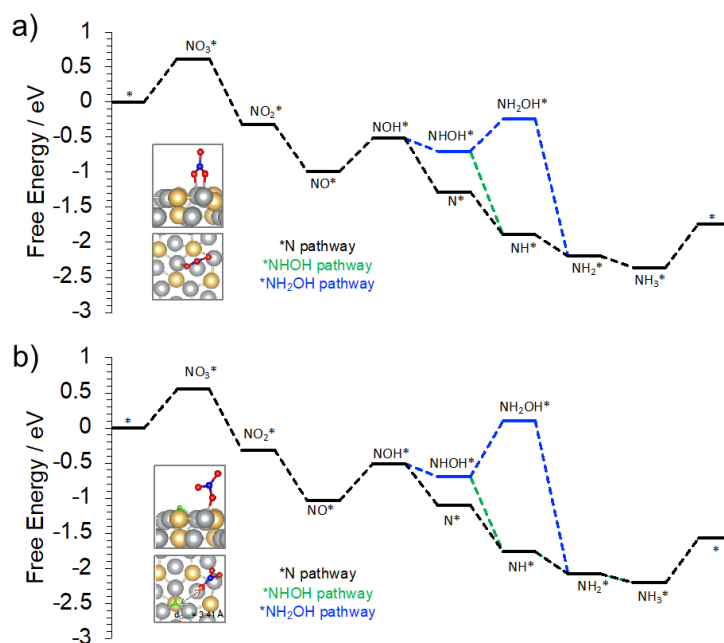
Figure S14. Free energy profiles for the nitrate reduction reaction on: **a)** A bare Ni_3P_2 terminated surface and **b)** A Ni_3P_2 terminated Ni_2P surface with co-adsorbed Hydrogen in the Ni_3 Hollow site. The reaction profiles are calculated at pH = 6.9 and T = 300 K. The pictorial inserts illustrate the change in the $Ni-NO_3$ coordination number following the co-adsorption of hydrogen going from bidentate ($\kappa^1-Ni_2O_2$) to a unidentate binding mode (κ^2-NiO).
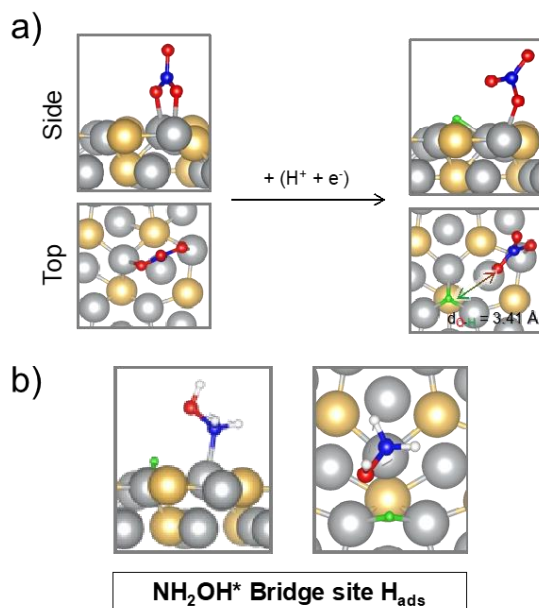

Figure S15. Top and side view following geometry optimization, highlighting the change in co-ordination of the surface adsorbed NO_3 species with the Ni_2P surface after the adsorption of co-adsorbed hydrogen in the Ni_3 hollow site, highlighting the change from a bidentate ($\kappa^1-Ni_2O_2$) to a unidentate binding mode (κ^2-NiO).

V.   Acknowledgements

VI. References

1 M. E. Mundy, D. Ung, N. L. Lai, E. P. Jahrman, G. T. Seidler and B. M. Cossairt, *Chem. Mater.*, 2018, **30**, 5373–5379.

2 F. G. Baddour, E. J. Roberts, A. T. To, L. Wang, S. E. Habas, D. A. Ruddy, N. M. Bedford, J. Wright, C. P. Nash, J. A. Schaidle, R. L. Brutchey and N. Malmstadt, *J. Am. Chem. Soc.*, 2020, **142**, 1010–1019.

3 Y. Zhu, J. Chen, D. Yuan, Z. Yang, X. Shi, H. Li, H. Jin and L. Ran, *TrAC Trends in Analytical Chemistry*, 2019, **119**, 115627.

4 D. Giustarini, R. Rossi, A. Milzani and I. Dalle-Donne, in *Methods in Enzymology*, Academic Press, 2008, vol. 440, pp. 361–380.

5 P. Giannozzi, S. Baroni, N. Bonini, M. Calandra, R. Car, C. Cavazzoni, D. Ceresoli, G. L. Chiarotti, M. Cococcioni, I. Dabo, A. D. Corso, S. de Gironcoli, S. Fabris, G. Fratesi, R. Gebauer, U. Gerstmann, C. Gougoussis, A. Kokalj, M. Lazzeri, L. Martin-Samos, N. Marzari, F. Mauri, R. Mazzarello, S. Paolini, A. Pasquarello, L. Paulatto, C. Sbraccia, S. Scandolo, G. Sclauzero, A. P. Seitsonen, A. Smogunov, P. Umari and R. M. Wentzcovitch, *J. Phys.: Condens. Matter*, 2009, **21**, 395502.

6 J. P. Perdew, K. Burke and M. Ernzerhof, *Phys. Rev. Lett.*, 1996, **77**, 3865–3868.

7 S. Grimme, *Journal of Computational Chemistry*, 2006, **27**, 1787–1799.

8 D. Joubert, *Physical Review B - Condensed Matter and Materials Physics*, 1999, **59**, 1758–1775.

9 H. J. Monkhorst and J. D. Pack, *Phys. Rev. B*, 1976, **13**, 5188–5192.

10 J. D. Head and M. C. Zerner, *Chemical Physics Letters*, 1985, **122**, 264–270.

11 I. Dabo, B. Kozinsky, N. E. Singh-Miller and N. Marzari, *Phys. Rev. B*, 2008, **77**, 115139.

12 O. Andreussi, I. Dabo and N. Marzari, *The Journal of Chemical Physics*, 2012, **136**, 064102.

13 I. A. Murphy, P. S. Rice, M. Monahan, L. P. Zasada, E. M. Miller, S. Raugei and B. M. Cossairt, *Chemistry of Materials*, 2021, **33**, 9652–9665.

14 J. K. Nørskov, J. Rossmeisl, A. Logadottir, L. Lindqvist, J. R. Kitchin, T. Bligaard and H. Jónsson, *J. Phys. Chem. B*, 2004, **108**, 17886–17892.

15 T. Hu, C. Wang, M. Wang, C. M. Li and C. Guo, *ACS Catalysis*, 2021, **11**, 14417–14427.